IOPscience iopscience.iop.org

Home Search Collections Journals About Contact us My IOPscience

Crystal structure and Ce valence variation in the solid solution $CeRh_{3-x}Pd_xB_{0.5}$

This content has been downloaded from IOPscience. Please scroll down to see the full text.

2014 Mater. Res. Express 1 016101

(http://iopscience.iop.org/2053-1591/1/1/016101)

View the table of contents for this issue, or go to the journal homepage for more

Download details:

IP Address: 131.130.28.161
This content was downloaded on 07/02/2014 at 14:55

Please note that terms and conditions apply.

Materials Research
Express

Crystal structure and Ce valence variation in the solid solution $CeRh_{3-x}Pd_xB_{0.5}$

I Zeiringer[1,2], J G Sereni[2], M G Berisso[2], K Yubuta[3], P Rogl[1], A Grytsiv[1] and E Bauer[4]

[1] Institute of Physical Chemistry, University of Vienna, Währingerstr. 42, A-1090 Wien, Austria
[2] Div. Bajas Temperaturas, CAB-CNEA, CONICET, 8400 Bariloche, Argentina
[3] Institute for Materials Research, Tohoku University, Sendai 980-8577, Japan
[4] Institute of Solid State Physics, Vienna University of Technology, Wiedner Hauptstr. 8-10, A-1040 Wien, Austria
E-mail: peter.franz.rogl@univie.ac.at

Received 22 October 2013, revised 6 November 2013
Accepted for publication 13 November 2013
Published 16 January 2014
Materials Research Express **1** (2014) 016101
doi:10.1088/2053-1591/1/1/016101

Abstract

Crystal structure and physical properties have been studied in the solid solution $CeRh_{3-x}Pd_xB_{0.5}$ ($x = 0$, 0.5, 1.2, 1.5, 1.7, 2.5, 3) in as-cast state by x-ray powder diffraction and scanning and high-resolution electron microscopy, as well as by low-temperature measurements of the magnetic susceptibility and specific heat. X-ray powder patterns of the alloys were indexed on the basis of a cubic primitive $AuCu_3$ lattice throughout the entire solution showing a monotonous increase in three regimes. For $0 \leqslant x \leqslant 1.5$, the volume increase corresponds merely to the substitution of Rh by Pd atoms, the sizes of which are rather close. In this regime the tetravalent character of cerium is unaffected. For $x > 1.5$, the lattice expansion becomes enhanced and is thus attributed to a gradual valence change of the Ce atoms (an intermediate valence regime). Finally, for $x > 2.4$, the system shows a predominant trivalent behavior. In this region, the specific heat coefficient reaches a value of 4.4 J mol^{-1} K^2, two orders of magnitude larger than that in the Rh-rich border. Selected area electron diffraction patterns of the $CeRh_{3-x}Pd_xB_{0.5}$ compounds revealed the appearance of ½ ½ ½-type superstructures and satellite reflections with respect to the parent $AuCu_3$ structure. Whereas the ½ ½ ½-type superstructure is confined to the Rh-rich part of the solid solution, satellite reflections are observed throughout the solid solution and hint towards the existence of a domain structure enclosed by anti-phase boundaries.

Keywords: cerium valence

© 2014 IOP Publishing Ltd

1. Introduction

A significant effort has been made during the last decades to study the rich variety of physical properties of the $CeTM_3$ family of compounds (where TM = Rh and Pd) and related systems like $CeRh_{3-x}Pd_x$ [1, 2]. Its simple cubic primitive $AuCu_3$ structure (defect perovskite) provides the possibility of incorporating light interstitial elements like B (in $CePd_3B_y$ [3–7], $CeRh_3B_y$ [3, 7, 8]), C (in $CeRh_3C_{1-y}$ [9, 10]), small amounts of Be (in $CePd_3Be_y$ [5, 11]) and Si (in $CePd_3Si_y$ [5, 7]).

One of the most interesting properties of these alloys is the possibility of studying, within a continuous alloy series, the electronic transition of Ce from its Ce^{4+} configuration to the Ce^{3+} one.

It is well known that crystal and electronic structures are intimately related, and the study of one of them has to be complemented by the knowledge of the other. Magnetic properties were preferably used to identify the electronic characteristics of materials, particularly for systems containing rare earth elements, able to adapt their electronic configuration to the volume (V_{av}) available within the crystal structure and consequently their valence (Z). Among such elements, cerium is known to adjust the occupation of its $4f^1$ orbital to the surrounding chemical potential (μ) through its local Z/V_{av} ratio modification. Concomitantly, the electronic configuration of Ce varies between a magnetic state (at $4f^1$ full occupation) and a non-magnetic state (for a $4f^{1-n}$ partial occupation). Consequently, these Ce-based compounds provide the unique possibility of tuning the Z/V_{av} ratio by changing μ or, inversely, to trace the variation of μ by measuring V_{av}. Indeed, for the alloy series $CeRh_{3-x}Pd_x$ and $CeAg_{3-z}Pd_z$ [2] a transition from the Ce^{4+} regime (Rh-rich) to the Ce^{3+} regime (Pd-rich) has already been monitored [12].

In order to better understand the aim of this work, a brief overview of the properties of the family of $CeTM_3B_y$ compounds related to this work is given in the following.

$CePd_3B_y$: The valence of Ce in $CePd_3B_y$ was found to increase in the concentration range $y < 0.4$ as the lattice volume increases with rising B content [3, 4, 6, 7]; it saturates at $y \sim 0.4$ once the Ce trivalent state is reached. Coincidentally, the lattice parameter also stops growing (see figure 1). Accordingly, low-temperature properties show that magnetic interactions develop some short-range order that increases in intensity up to $y = 0.35$ [4]. Unexpectedly, for $y > 0.4$ the specific heat anomaly related to those short-range correlations smears out and transforms into a continuous increase of C_m/T as temperature decreases [5]. The strengthening of magnetism observed for $CePd_3B_y$ at $y \sim 0.25$ was backed by specific-heat measurements [4, 13, 14]. X-ray photoemission, Bremsstrahlungs–Isochromat and electron energy-loss spectroscopy [15] revealed a $4f^n$ occupation varying from $n_f \sim 0.9$ in $CePd_3$ to $n_f \sim 1$ in $CePd_3B$ at 90 K and an almost constant hybridization of f-electrons with conduction electrons ($\Delta = 150 \pm 20$ meV).

Phase equilibria studies in the system Ce-Pd-B at 850 °C [16] defined the extension of the homogeneity range of $CePd_3B_y$ for $0 \leqslant y \leqslant 0.65$ at 850 °C, limiting the boron incorporation to 13 atomic % B [16]. Alloys with $y \leqslant 0.15$ behave as a Kondo lattice, whereas the behavior for $y > 0.2$ becomes completely different, tracking the valence change of Ce. Concerning transport properties, $CePd_3$ ranks among the materials with the highest Seebeck coefficients (110–120 μV K^{-1} around 150 K) amid correlated thermoelectric systems [17, 18]. Boron incorporation leads to a strong decrease of the Seebeck coefficient (~40 μV K^{-1} around 150 K for $CePd_3B_{0.1}$) [17, 18], but also to a large drop of the phonon thermal conductivity, attributed to the rattling modes of the loosely bonded B atoms [17].

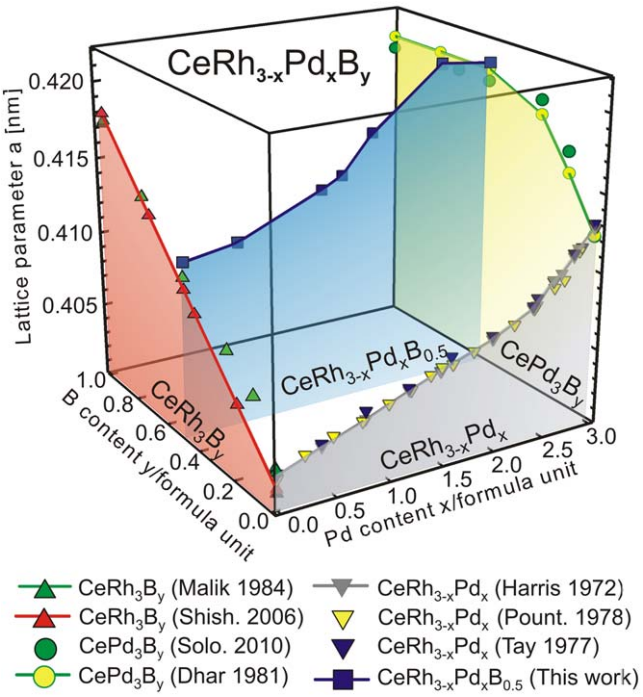

Figure 1. Lattice parameter vs Pd content x and B content y for $CeRh_{3-x}Pd_xB_y$.

The observed disappearance of magnetic correlations for $y > 0.4$ is an open question, tentatively attributed to atomic disorder produced by the random distribution of interstitial B atoms.

$CeRh_3B_y$: Lattice parameters as a function of the incorporation of boron in $CeRh_3$ were found to increase almost linearly with increasing boron content [7, 19], whereas the magnetic susceptibility of $CeRh_3$ is almost temperature independent down to 50 K [1, 7], consistent with Pauli-paramagnetic behavior and suggesting a tetravalent state of Ce [7]. Correspondingly, the valence of cerium changes from Ce^{4+} in $CeRh_3$ [1, 7] to a mixed valency in $CeRh_3B$ [7, 10]. The lattice parameters of $CeRh_3B$, determined by Takei *et al* [20] in as-cast state and after annealing at 1400 °C, exhibit a difference probably due to slightly different atomic arrangement. Shishido *et al* [19] observed an anomalous drop of the Vickers hardness around $y = 0.444$. An electron diffraction (ED) and high-resolution electron microscopy (HRTEM) study of the crystal structure of $CeRh_3B_{0.5}$ by Yubuta *et al* [8] revealed ½ ½ ½-type superlattice reflections and fine satellite reflections around all reflections. The new superstructure is formed by an ordered arrangement of B atoms and is modulated by the appearance of fine domains with an average size of ~3 nm [8]. The authors suggested that the weakness of chemical bonding strength in the boundaries between the fine domains causes the anomalous decrease of hardness in the region of the new structure [21]. *Ab initio* calculations of the atomic and electronic structure and the elastic properties of $CeRh_3B_y$ revealed (i) a strong covalent bonding between boron 2*p* and Rh 4*d* electrons, (ii) the Fermi level in a pseudogap and (iii) a significant *f*-*d* hybridization [22].

$CeRh_{3-x}Pd_xB_y$: Measurements of magnetic susceptibility and lattice parameters for the $CeRh_{3-x}Pd_x$ alloy [1, 23] indicated Ce to be in the tetravalent state for the composition range $0 \leqslant x \leqslant 2.4$, whereas with increasing x the effective valency decreases to intermediate valence

values at $CePd_3$ [1]. Consistently, L_{III} x-ray absorption edge measurements revealed an increase in the valence of Ce between $CePd_3$ and $CeRh_{1.2}Pd_{1.8}$, but a constant value for higher Rh contents [24]. From temperature-dependent resistivity and Ce-L_{III}-valence-state measurements, Perez and coworkers [3] concluded that the solid solution $CeRh_{3-x}Pd_xB$ passes continuously from a Kondo local-moment regime ($0 \leqslant x \leqslant 0.6$) to a mixed valent regime ($0.6 < x \leqslant 2.1$) and further to a saturated valence regime ($2.1 < x \leqslant 3$).

The purpose of this work is an attempt to expand the $AuCu_3$ lattice of $CeRh_{3-x}Pd_x$ alloys by Boron addition in order to tune the electronic configuration from $4f^0$ towards $4f^1$. Such a transformation cannot be completed by a simple Rh/Pd substitution because $CePd_3$ is in an intermediate valence state. By adding more conduction electrons to the band (e.g., by a Pd/Ag substitution), the Ce valence variation can be driven up to the Ce^{3+} configuration. Boron incorporation, however, promotes a shift of the Rh/Pd electronic substitution effect to lower the Rh content because of the B-driven lattice expansion. Once tuned at the proper B concentration, this shift should allow the full Ce^{4+} to Ce^{3+} transformation into the unique Rh to Pd range, avoiding the extension into the Pd by Ag substitution.

With respect to the incipient short-range magnetic order observed in $CePd_3B_y$ up to $y = 0.35$—which vanishes for $y > 0.4$—it is necessary to elucidate whether or not short-range order is an atomic disorder effect or has an intrinsic origin. To that respect one can mention that the heavy fermion behavior of $CePd_3B_{0.6}$ was improved after annealing [4, 11]. For such a purpose a detailed structure investigation concerning boron/vacancy ordering was carried out in this work, to better control the degree of disorder introduced by doping. Taking profit of previous investigations on $CeRh_3B_{0.5}$ [8], which evidenced a ½ ½ ½–type superstructure, the alloy system with the $CeRh_{3-x}Pd_xB_{0.5}$ was chosen for this investigation.

Thus the aim of this work is two-fold: (a) to determine the valence instability region of Ce within the solid solution $CeRh_{3-x}Pd_xB_{0.5}$, in combination with (b) a detailed study of the influence of atom ordering (superstructures and antiphase domains) on the evolution of physical properties. For this purpose we have investigated a series of samples with $x = 0$, 0.5, 1.5, 2.5, 3, using x-ray powder diffraction, scanning and high-resolution electron microscopy, and by magnetic susceptibility as well as magnetization and heat-capacity measurements down to very low temperatures.

2. Experimental details

Polycrystalline samples of about 1 g were prepared by a standard arc melting technique under argon. Powders of rhodium (purity 99.99%) and/or palladium (purity 99.99%) and crystalline boron (purity 98–99%) were carefully mixed in stoichiometric ratios, compacted and melted before adding the appropriate amount of cerium (purity 99.9%). The molten buttons were turned over and remelted at least three times to ensure homogeneity with weight losses smaller than 1 mass % in all cases.

For sample characterization, scanning electron microscopy (SEM), electron probe microanalysis (EPMA) on a Zeiss Supra 55 VP operated at 20 kV using EDX detection for the quantitative analysis, and x-ray powder diffraction (XPD) with a Guinier–Huber image plate recording system (Cu-Kα_1 radiation) were used. Details of the characterization techniques can be found in a previous paper [25].

Selected-area electron diffraction (SAED) patterns with the incident beams along the directions [001], [011] and [111] were obtained using a 200 kV electron microscope (JEOL JEM-2000EXII). High-resolution electron microscopy (HREM) images were taken with a 200 kV electron microscope (TOPCON EM-002B). Precession electron diffraction (PED) patterns were obtained by using a Spinning Star (NanoMEGAS) device with a precession angle of 3.0°.

Magnetic measurements were performed using a Superconducting Quantum Interference Device (SQUID) running between 1.8 K and room temperature, and with applied magnetic fields up to 5 T. Specific heat was measured between 0.5 and 30 K using a standard heat pulse method with $\Delta T/T \approx 1\%$. A reference sample of $LaPd_3B$ [11] was used to evaluate the phonon contribution and extract the magnetic specific heat as $C_m = C_{meas} - C_p(La)$.

3. Results

3.1. Homogeneity range of the solid solution $CeRh_{3-x}Pd_xB_y$

Samples of the solid solution $CeRh_{3-x}Pd_xB_{0.5}$ ($x = 0$, 0.5, 1.2, 1.5, 1.7, 2.5, 3) have been studied by XPD and EPMA in the as-cast state. X-ray powder patterns of the alloys were indexed on the basis of a cubic primitive $AuCu_3$ lattice (space group $Pm\bar{3}m$; $a_0 \sim 0.4$ nm). The dependency of the lattice parameters, a, of the solid solution $CeRh_{3-x}Pd_xB_y$ ($AuCu_3$ type) with increasing Pd content, x, and increasing B content, y, is given in figure 1, in comparison with data available from the literature. On the pure Rh side of the figure, a linear increase of the lattice parameter with increasing B content has been reported by Shishido and coworkers [19] for $CeRh_3B_y$. This parameter ranges from $a = 0.4015(1)$ nm ($y = 0$) to $a = 0.4180(1)$ nm ($y = 1$) for alloys annealed at 1300 °C, whereas the lattice parameters determined by Malik *et al* [7] for alloys in as-cast state show deviations from linearity at low B content. In this area ($y = 0.12$ and 0.25), the authors [7] observed a splitting of the peaks in the x-ray powder pattern whereby one set of lines could be fitted with the lattice parameter of $CeRh_3$ and the other with an expanded lattice (see figure 2). The rather large difference of the lattice parameters in as cast state ($a = 0.4147$ nm) and after annealing at 1400 °C ($a = 0.4213$ nm) reported by Takei *et al* [20] for $CeRh_3B$, might be due to different compositions. For comparison, on the axis without B content, i.e., $CeRh_{3-x}Pd_x$, the lattice parameters increase linearly between $x = 0$ and $x = 2.4$ and between $x = 2.4$ and $x = 3$ [1, 23, 26] as previously reported. Even $Ce_{1-u}Pd_{3+u}$ has a small homogeneity range [27] extending from stoichiometric $CePd_3$ ($a = 0.4129(2)$ nm) to $Ce_{0.92}Pd_{3.08}$ ($a = 0.4112(2)$ nm) at 800 °C [27]. The lattice parameters of the solid solution $CePd_3B_y$ increase with increasing B content up to $y = 0.4$ ($a = 0.4203$ nm) in as-cast alloys [6] and up to $y = 0.25$ ($a = 0.419\,54(5)$ nm) [16] for samples annealed at 850 °C, but saturate for higher boron content. The maximum solubility of boron in this solid solution was found to be about 13 atomic % B ($y = 0.65$) [16].

For the solid solution $CeRh_{3-x}Pd_xB_{0.5}$ ($x = 0$, 0.5, 1.2, 1.5, 1.7, 2.5, 3), investigated in this work, lattice parameters increase slightly with increasing Pd content from $a = 0.411\,47(5)$ nm ($x = 0$) to $a = 0.415\,01(5)$ nm ($x = 1.5$), followed by a strong increase up to $a = 0.421\,04(6)$ nm ($x = 2.5$) and a slight decrease afterwards to $a = 0.420\,73(2)$ nm ($x = 3$; see figure 1). Our lattice parameters of $CeRh_3B_{0.5}$ and $CePd_3B_{0.5}$ are slightly larger but are still in good agreement with the literature data. The results of XPD and EPMA are summarized in table 1. Only the metal ratios were measured over several areas, as it is not possible to precisely and reliably determine

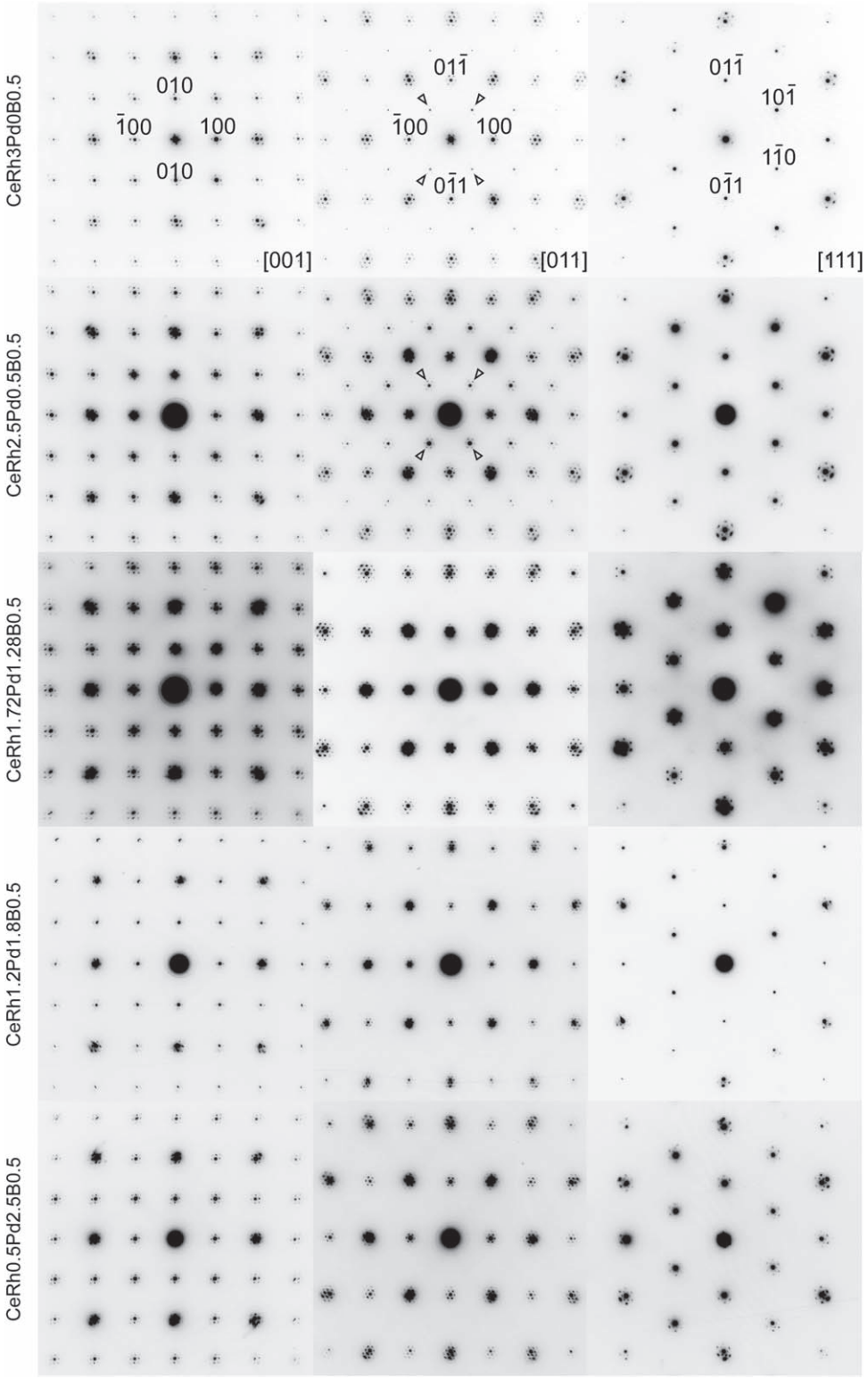

Figure 2. SAED patterns of the $CeRh_{3-x}Pd_xB_{0.5}$ compounds, taken with an incident beam parallel to the directions [001] (left), [011] (center) and [111] (right). Reflections are indexed on the basis of the $AuCu_3$-type structure.

Table 1. Results of XPD, EPMA and ED measurements.

Nominal composition	Composition from EPMA	a_{AuCu_3} [nm]	½ ½ ½ superstructure reflections	Satellite reflections
$CeRh_3B_{0.5}$	$CeRh_3$	0.411 47(5)	yes	yes
$CeRh_{2.5}Pd_{0.5}B_{0.5}$	$CeRh_{2.5}Pd_{0.5}$	0.412 49(5)	yes	yes
$CeRh_{1.7}Pd_{0.3}B_{0.5}$	$CeRh_{1.7}Pd_{0.3}$	0.414 33(2)	no	yes
$CeRh_{1.5}Pd_{1.5}B_{0.5}$	$CeRh_{1.5}Pd_{1.5}$	0.415 01(5)	-[a]	-[a]
$CeRh_{1.2}Pd_{1.8}B_{0.5}$	$CeRh_{1.2}Pd_{1.8}$	0.417 41(3)	no	yes
$CeRh_{0.5}Pd_{2.5}B_{0.5}$	$CeRh_{0.5}Pd_{2.5}$	0.421 04(6)	no	yes
$CePd_3B_{0.5}$	$CePd_3$	0.420 73(2)	no	Yes

[a] not investigated.

the small B content by EPMA. The lattice parameters are given for the cubic $AuCu_3$ parent type from which any possible superstructures can be derived.

3.2. Electron diffraction studies on the solid solution $CeRh_{3-x}Pd_xB_{0.5}$

SAED patterns of the $CeRh_{3-x}Pd_xB_{0.5}$ compounds, taken with an incident beam along the directions [001] (left), [011] (centre) and [111] (right), are shown in figure 2. Reflections are indexed with respect to the $AuCu_3$-type structure. The presence of ½ ½ ½-type superstructure and satellite reflections is summarized in table 1.

3.2.1. ½ ½ ½-type superstructure reflections. As indicated by the arrowheads in figure 2, ½ ½ ½-type superstructure reflections are observed only in $CeRh_3B_{0.5}$ and $CeRh_{2.5}Pd_{0.5}B_{0.5}$. Therefore, the ½ ½ ½-type superstructure, which has been discussed in detail for $CeRh_3B_{0.5}$ [8], might be dominant only in the Ce–Rh–B system.

3.2.2. Satellite reflections. For all compounds investigated, many fine satellite reflections appear around the Bragg reflections. The characteristic features of the satellite spots are significant and similar to those of the $CeRh_3B_{0.5}$ compound [8]. It is reasonable to consider that the fine satellite reflections indicate the existence of a domain structure enclosed by anti-phase boundaries. The appearance of only satellite reflections without superstructure reflections has not been observed in the ternary solid solution $CeRh_3B_x$. Figure 3 shows HREM images of (a) $CeRh_{2.5}Pd_{0.5}B_{0.5}$ with the ½ ½ ½-type superstructure reflections and (b) $CeRh_{1.7}Pd_{1.3}B_{0.5}$ without the ½ ½ ½-type superstructure reflections, taken with the incident beam parallel to the [011] direction, and PED patterns in insets. In the images, one can see a modulation with a domain structure, which is similar to that of $CeRh_3B_{0.5}$. At the boundaries between the domains, one can see anti-phase displacements of lattice fringes and dislocation-like defects.

3.3. Magnetic susceptibility

The low-temperature magnetic properties of this system are summarized in figure 4 in a double logarithmic representation. Starting from the Pd-rich side, the magnetic susceptibilities ($M/B = \chi$) of $CePd_3B_{0.5}$ and $CeRh_{0.5}Pd_{2.5}B_{0.5}$ follow the Curie–Weiss (C–W) law above about 50 K. Deviations below that temperature can be attributed to a reduction of the thermal-driven

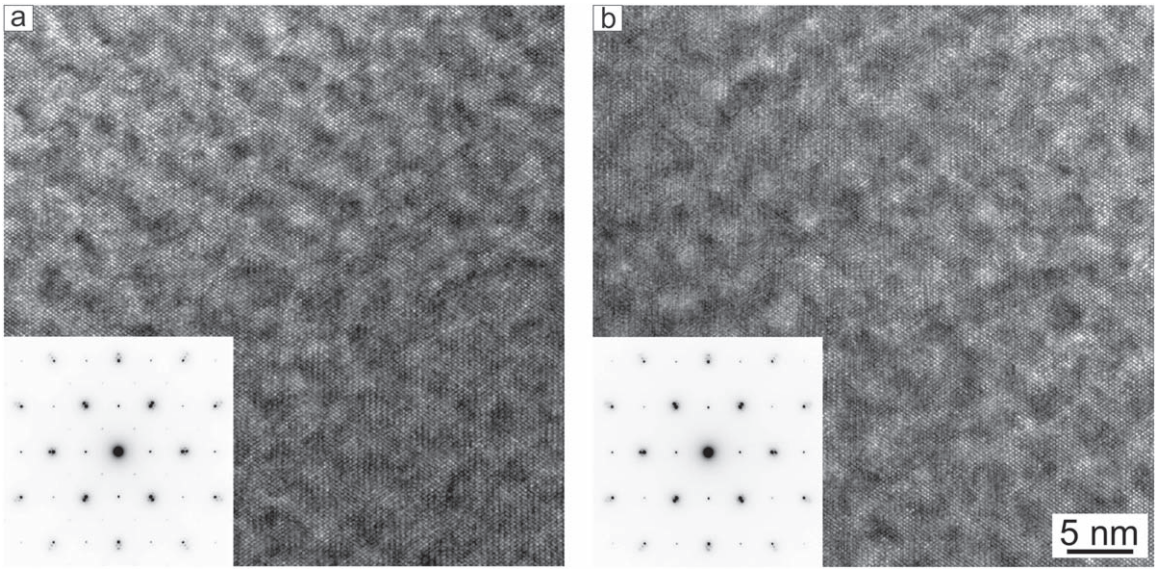

Figure 3. HREM images and corresponding PED pattern taken with the incident beam parallel to the [011] direction (inset) of (a) $CeRh_{2.5}Pd_{0.5}B_{0.5}$ and (b) $CeRh_{1.7}Pd_{1.3}B_{0.5}$.

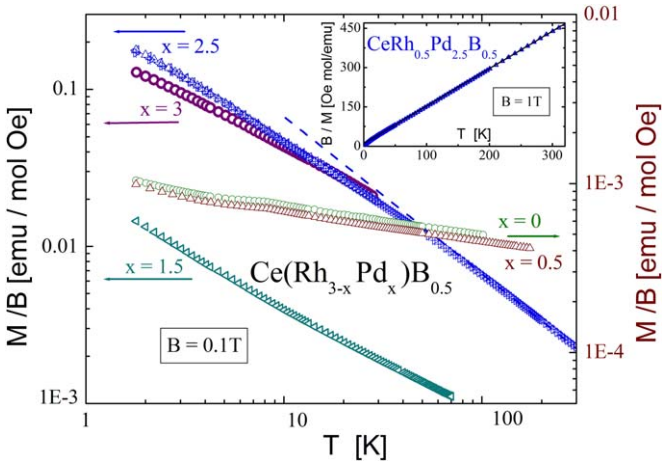

Figure 4. Temperature dependence of the magnetic susceptibility in a double logarithmic representation. The left axis is for $x \geqslant 1.5$ samples and the right axis is for Rh-rich alloys. Inset: inverse susceptibility of sample $CePd_{2.5}Rh_{0.5}B_{0.5}$ showing a Curie–Weiss behavior.

occupation of the excited crystal electric field (CEF) levels. This behavior is also depicted in the inset as a standard $1/\chi$ representation, where the solid line represents the C–W law with the Curie constant $C = 0.7$ emuK mol^{-1}, corresponding to an effective moment $\mu_{\mathrm{eff}} = 2\ \mu_{\mathrm{B}}$, and a paramagnetic Curie temperature $\theta_{\mathrm{P}} = -7$ K. The effective magnetic moment observed is about 20% lower than the value expected for a Ce^{3+} ion $g_J \mu_{\mathrm{B}} [J(J+1)]^{1/2} = 2.54\ \mu_{\mathrm{B}}$. This value, together with $\theta_{\mathrm{P}} = -7$ K suggests a weak Kondo effect being present in both the ground state (GS) and excited CEF levels.

The intermediate concentration sample $CeRh_{1.5}Pd_{1.5}B_{0.5}$ shows a drastic reduction of the magnetic signal (see also figure 4) that can be described by a C–W law with $\mu_{\mathrm{eff}} = 0.4\ \mu_{\mathrm{B}}$ and

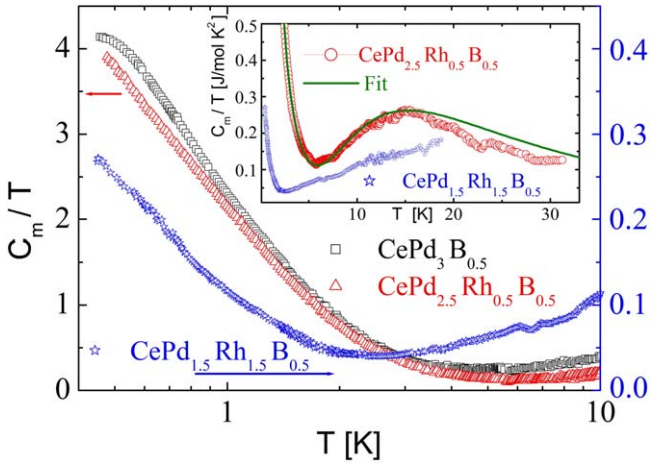

Figure 5. Temperature dependence of the magnetic contribution to specific heat divided by temperature in a semi-logarithmic representation showing the different temperature dependencies between both Pd-rich samples on the left axis. the right axis refers to the $x = 1.5$ alloy. Inset: high temperature specific heat of two Rh/Pd alloys. A continuous curve fits C_m/T of $CeRh_{0.5}Pd_{2.5}B_{0.5}$ as a sum of a non-Fermi-liquid ground state and standard Shottky anomalies for the CEF levels; see the text.

$\theta_P = -90$ K. Both the reduction of the Ce magnetic moment and the strong increase of $|\theta_P|$ up to 90 K indicates a dominant Kondo regime for this composition.

On the Rh-rich side, a nearly-temperature-independent susceptibility is observed. The experimental results can be described as $\chi = \chi_0 + C_i/T$ with $\chi_0 = 0.33\ 10^{-3}$ emu mol^{-1} and C_i as a contribution from magnetic impurities, equivalent to about 100 ppm Gd atoms. The value derived for χ_0 of $CeRh_3B_{0.5}$ is slightly larger than for $CeRh_{2.5}Pd_{0.5}B_{0.5}$, but within the indetermination of this simple description.

3.4. Specific heat

In figure 5 the magnetic contribution to the specific heat (C_m) for $x \geqslant 1.5$ samples is presented. Pd-rich alloys show record high values of C_m/T for $T \to 0$, with $CePd_3B_{0.5}$ exceeding 4 J mol K^{-2} at $T = 0.5$ K. Such a value is outnumbered only by $CeNi_9Ge_4$ [28] at lower temperatures because in this compound the first CEF excited doublet contributes to C_m/T even at very low temperatures. Notably, $CePd_3B_{0.5}$ and $CeRh_{0.5}Pd_{2.5}B_{0.5}$ show a clear functional difference in their C_m/T thermal dependencies below about 0.7 K, the former with a tendency to saturation at very low temperature, whereas the latter follows a well defined logarithmic dependence. Such a difference was previously observed between stoichiometric $CeNi_9Ge_4$ and doped with a few atomic % of La [28]. This significant change in behavior can be attributed to the difference between a coherent (or lattice) behavior and the loss of coherence due to local Rh/Pd atomic disorder.

At higher temperature ($T > 7$ K), C_m/T shows a maximum at about 15 K (see insert in figure 5). This thermal dependence is tentatively ascribed to the contribution of CEF levels centered at 23 K and 31 K, respectively (solid line, inset of figure 5). Since a standard Schottky anomaly is computed on the basis of well-defined levels, the significant overlap between both anomalies suggests that the actual excited CEF level can be a hybridized Γ_8 quartet with an associated Kondo temperature of $T_K \approx 8$ K, which is compatible with the value of $|\theta_P|$

observed for that sample. Such a four-fold degenerated CEF level is expected in fcc crystal symmetry [32] for a $J = 5/2$ ion like Ce; the doublet Γ_7 would then be the ground state. In such a case, the CEF splitting can be evaluated as $\Delta = 0.43\ T_{max} \approx 30$ K, T_{max} being the temperature of the maximum of $C_m(T)$. Notice that in figure 5, C_m/T results for $CeRh_{1.5}Pd_{1.5}B_{0.5}$ are referred to the right axis because of the significant reduction of its electronic density of states. Rh-rich samples are not included in figure 5 because their small C_m/T values could hardly be observed in the graph.

4. Discussion

4.1. Crystal chemistry

The group–subgroup relations for perovskite ($CaTiO_3$) and its large number of derivative structure types have been shown by Bock and Müller [29] in the form of several Bärnighausen trees, classified after coordination octahedra, Jahn Teller distortion, substitution variants or distortion variants. One small part of the Bärnighausen tree is shown in figure 6, relevant to the defect-ordered structure types among borides.

The ordering of B-atoms and vacancies in Zr_2Ir_6B [30] and Ti_2Rh_6B [31] leads to an eight times larger unit cell ($a = b = c = 2a_0$; space group $Fm\bar{3}m$, K_2PtCl_6 type; see figure 7), which has been defined for these compounds by x-ray single-crystal studies. As the ½ ½ ½ superstructure reflections in the SAED pattern of $CeRh_3B_{0.5}$ are relatively strong, Yubuta *et al* independently suggested that in this structure besides the boron ordering, displacements of the Rh atoms around the B atoms also appear [8]. Another possibility for B/vacancy ordering would exist in the $K_2OsCl_4O_2$ structure type with lower tetragonal symmetry ($a = b = \sqrt{a_0}$, $c = 2a_0$, space group *I*4/*mmm;* see figure 7).

In the system under study, the ½ ½ ½ superlattice reflections, leading to an enlargement of the unit cell, are clearly visible for $CeRh_3B_{0.5}$ and $CeRh_{2.5}Pd_{0.5}B_{0.5}$ on the SAED pattern. This is in contrast to Zr_2Ir_6B, for which the reflections caused by the ordering are also visible on the x-ray powder spectrum [30]. Figure 7 shows the Rietveld refinement of the x-ray powder pattern for $CeRh_{2.5}Pd_{0.5}B_{0.5}$, including Miller indexes (bars), for the simple $CaTiO_3$ type and the K_2PtCl_6 type. In the case of $CeRh_3B_{0.5}$ or $CeRh_{2.5}Pd_{0.5}B_{0.5}$, the small reflections found on the powder patterns in addition to those of the parent $AuCu_3$-type can not be unambiguously attributed to the superstructure, but along with the results of the electron diffraction, the K_2PtCl_6 structure type can be considered.

4.2. Entropy

In the inset of figure 8, the thermal variation of the entropy (S_m) of $CeRh_{0.5}Pd_{2.5}B_{0.5}$ and $CeRh_{1.5}Pd_{1.5}B_{0.5}$ are presented. Since the former alloy shows a high value of $C_m(T \to 0)/T$, in order to recognize up to which extent such a value corresponds to a Kramer's doublet GS only, a more quantitative inspection of the $C_m(T)/T$ dependence of the GS contribution is required. Experimental data can be properly fitted with a modified power law (MPL) of the form $C_m/T = g/(T^Q + A)$ [32], where the ratio $g/A = C_m/T$ $(T \to 0)$ and A is an energy scale for the deviation from a pure power law. The present results are well fitted with $g/A = 4.8$ J mol^{-1} K^2, $A = 0.9$ K and $Q = 2.1$ for the ground state doublet (see the solid line in figure 8). Above about

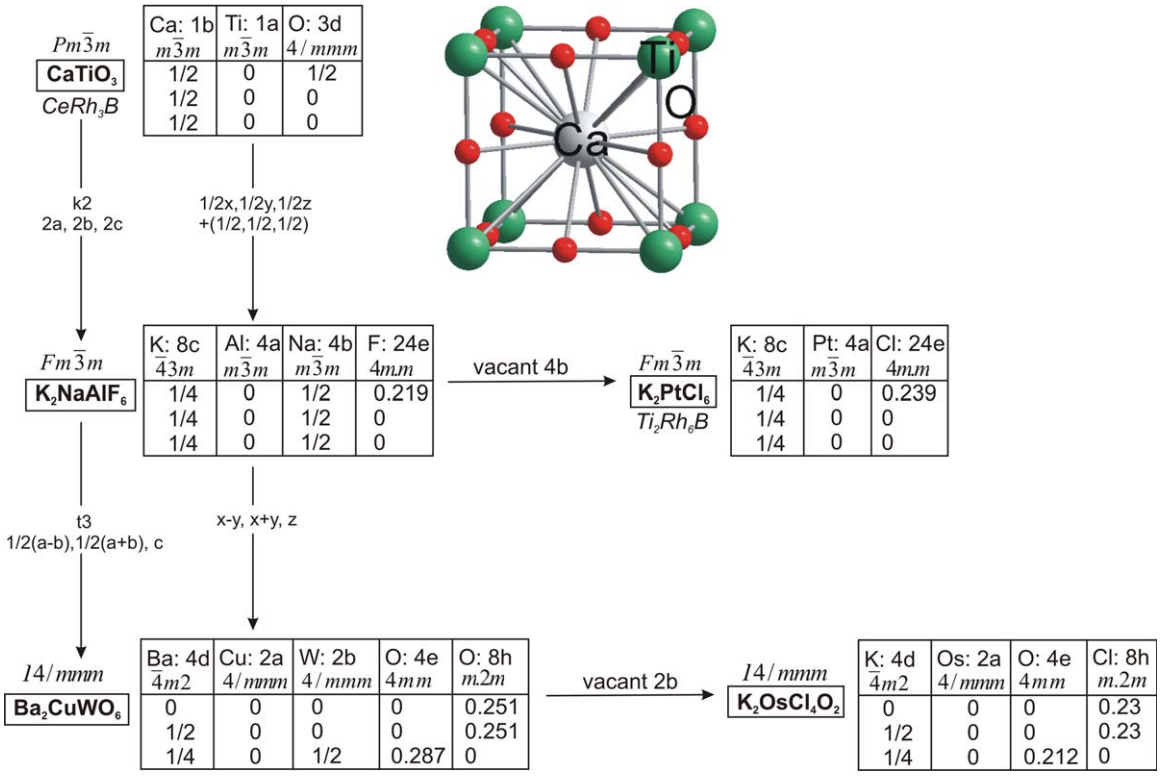

Figure 6. Branch of the Bärnighausen tree of the perovskite family including ordered defect structures.

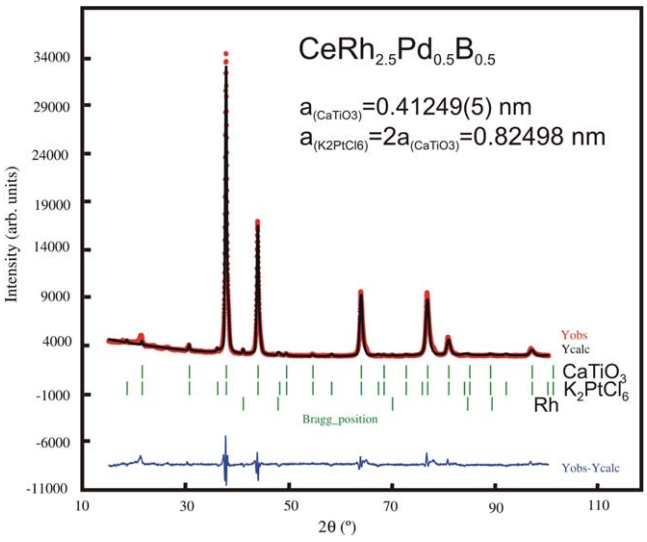

Figure 7. Rietveld refinement for $CeRh_{2.5}Pd_{0.5}B_{0.5}$ including the simple $CaTiO_3$ type and the K_2PtCl_6 type.

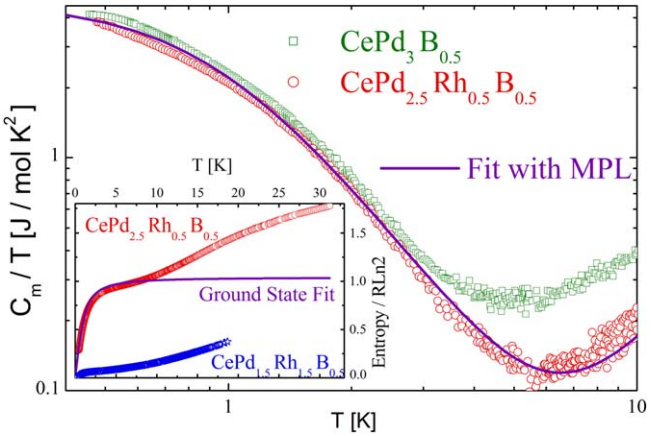

Figure 8. Temperature dependence of the magnetic contribution to specific heat divided by temperature in a double logarithmic representation showing the fit with a modified power law (MPL), plus a CEF contribution for $CePd_3B_{0.5}$ (see the text). Inset: entropy gain showing the difference between the GS (solid line) and CEF contribution for $CeRh_{0.5}Pd_{2.5}B_{0.5}$ compared with $CeRh_{1.5}Pd_{1.5}B_{0.5}$.

4 K the CEF contribution becomes relevant, and is properly described taking into account a CEF splitting of ≈30 K, as discussed for the inset of figure 5.

There is a thermodynamic constraint to be fulfilled by the MPL parameters originated in the entropy of the doublet GS: $S(T_7) = R\ln 2$. According to that, the continuous curve in the inset of figure 8 shows how the integral of $C_m(T)/T = g/(T^Q + A)$ saturates at that value. The entropy exceeding Rln 2 corresponds to a contribution of the excited Γ_8 CEF level, located around 30 K above the ground state. At the upper temperature limit of our experimental range (≈30 K), $S_m(T)$ reaches the value ≈1.8 Rln 2, which is a fraction of the total entropy Rln 6 expected for the six-fold degenerated Hund's rules ground state of Ce (i.e., $2J + 1 = 6$ for $J = 5/2$).

In the case of $CeRh_{1.5}Pd_{1.5}B_{0.5}$, the scenario changes completely because its specific heat is reduced by more than one order of magnitude and consequently its magnetic entropy (S_m) increases very slowly, as shown in the inset of figure 8. With such a modest increase of $S_m(T)$, the Rln 2 value is shifted to higher temperatures, quite above the excited CEF level. Furthermore, this CEF level will also progressively contribute to enlarge S_m towards an upper value of Rln 6 (if the Γ_8 quartet is taken into account). This fact, and the strong increase of $|\theta_P|$ ≈90 K (see subsection 3.3), are typical signatures for intermediate valence behavior, where the CEF level width overcomes the CEF splitting [33].

There is, however, an unexpected but robust increase of $C_m(T)/T$ below about 2 K in this alloy, as shown in figure 5. In terms of entropy, this contribution can be evaluated to be about 7% of Rln 2. Such a value is extracted applying the same procedure as that applied for the analysis of $S_m(T)$ of $CeRh_{0.5}Pd_{2.5}B_{0.5}$ performed in the inset of figure 8. The value also agrees with the reduction of the Curie constant extracted from figure 4. The low energy scale of this contribution (arising below about 2 K) may be originated by the random distribution of Pd/Rh atoms. Although the atomic distribution in an alloy is expected to deviate to some extent from the ideal value, a random distribution (Pd/Rh in this case) implies, however, that in this system the density of states increases exponentially on the Pd-rich side by about two orders of magnitude when compared with the Rh-rich side. Even involving only 7% of Rln 2, any Pd-rich cluster would surpass the respective contribution of a Rh-rich equivalent. Nevertheless, such a

well-defined increase as in $CeRh_{1.5}Pd_{1.5}B_{0.5}$ is quite unexpected in terms of a random distribution, and a more intrinsic effect cannot be excluded.

Apart from its high value for a doublet ground state, the record of $C_m(T)/T$ $(T \to 0) = 4.8$ J mol^{-1} K^2 has relevant physical implications. Compared with standard Fermi liquids like $CeRh_3$ with $\gamma = 0.014$ J mol^{-1} K^2 [34], it represents an increase of about 300 times in the density of states and the concomitant decrease of the characteristic energy scale, down to a few degrees. These two alloys show thermal C_m/T dependencies typically observed in the vicinity of quantum critical points. In fact, the $C_m(T)/T = -a \log(T_0/T)$ dependence of $CeRh_{0.5}Pd_{2.5}B_{0.5}$ scales with other alloyed Ce systems [35], but exhibits an even lower T_0 value than the exemplary system $CeCu_{5.9}Au_{0.1}$ [36]. Stoichiometric $CePd_3B_{0.5}$, however, shows a power law thermal dependence above 1 K with a clear tendency to saturation below that temperature. This experimental result can be properly described by a modified power law like $C_m(T)/T = 4.4/(T^{2.1} + 0.9)$, with an exponent $Q \sim 2$ and an A term that accounts for the saturation effect at $T \to 0$. These types of behaviours are generally recognized as non-Fermi-liquids, arising from an increasing density of excitations as the temperature tends towards zero. Since those excitations are not necessarily distributed in a continuous spectrum of energy, they cannot be considered to form an electronic band. Nevertheless, this particular value of $Q \sim 2$, gives the possibility to approximate the $T \to 0$ limit as $C_m(T)/T = (g/A)\,[1-(T/A)^2]$, which corresponds to a standard Fermi liquid system. In such a case $CePd_3B_{0.5}$ would be the compound with the highest known density of states or, equivalently, the narrowest electronic band reported. The feasible formation of an electronic band, however, has to be confirmed by transport measurements which should show, for example, a $\rho \sim T^2$ dependence below about 0.6 K where the Fermi liquid ground state may form.

4.3. Electron density and volume effects

As mentioned before, atomic valence and volume are intimately related parameters through the Coulomb potential acting on the valence electrons of the atoms. Stable valent elements participate in compound formation when their Wigner–Seitz cell border is compatible with those of the neighboring ligand atoms within an appropriate crystalline structure. Although the equilibrium values for these parameters have some range of flexibility, they are more restricted in ionic and covalent compounds than in intermetallics. That flexibility allows large families of compounds to form, with the same composition and structure, within an ample range of volume variation as typically observed in trivalent rare earth (RE^{+3}) compounds.

Certain elements, known to exhibit valence instabilities, are capable of accessing different electronic configurations compatible with different states of valence. Those elements, in general, form a large number of compounds, because they can adapt their valence/volume ratio (Z_{eff}/V_{av}) to those of the neighboring ligand atoms. Since ligand electrons are those from the valence band, in the case of Ce^{3+} only the [$6s^2 5d^1$] electrons participate in bonding; the $4f^1$ orbital is excluded due to its strong localized character. In contrast, in the case of Ce^{4+}, with the $4f^0$ electronic configuration, also a fourth delocalized electron may form the conduction band. Since the Ce^{3+} band, with an electronic structure [$6s^2 5d^1$], is the same as that of La^{3+}, the existence of isotypic La compounds indicates that the electronic band of Ce atoms is compatible with a Ce^{3+} state. On the other hand, if isotypic Zr^{4+} compounds form with a [$6s^2 5d^2$] band, like, e.g., $ZrFe_2$, $ZrCo_2$ Laves phases or $ZrRh_3$ (for the present case), it indicates that in the isotypic compounds the Ce electronic configuration is compatible with a Ce^{4+} state.

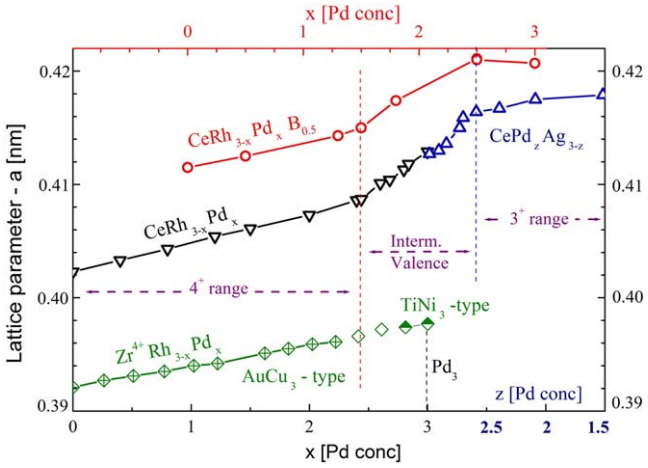

Figure 9. Variation of lattice parameters ($AuCu_3$-unit cell) for the alloy series $ZrRh_{3-x}Pd_x$, $CeRh_{3-x}Pd_x$, $CeRh_{3-x}Pd_xB_{0.5}$ and $CeAg_{3-z}Pd_z$ as a function of the Pd-content. The individual lattice parameter curves are shifted with respect to each other to comply with the region of Ce-intermediate valence and the transition from the Ce^{4+} to the Ce^{3+} regime.

The possibility of having intermediate valence states allows Ce atoms to adjust their Z_{eff}/V_{av} ratio as occurs in the $CeRh_{3-x}Pd_x$ alloy above $x = 2.4$, whereas the stable valent Zr cannot do this, as in $ZrRh_{3-x}Pd_x$, where a change of structure (i.e., V_{av}) occurs [26].

A further characteristic of the elements with valence instabilities is to adapt their Z_{eff}/V_{av} ratio to chemical potential modifications, allowing the stability of a crystalline structure in an extended range of concentrations like in $CeRh_{3-x}Pd_x$. This possibility contrasts with $ZrRh_{3-x}Pd_x$, included in figure 9, because the stable valence of Zr^{4+} constrains the system to modify the crystal structure from $AuCu_3$ to $TiNi_3$, once the available atomic volume V_{av} of Zr becomes mismatched with the neighboring electronic conditions. There is a useful heuristic constant provided by the product $Z_{eff} \times V_{av}$ (i.e., the effective valence Z_{eff} times the available volume) for this analysis because for metallic Ce, $Z_{eff} \times V_{av} \approx 80$ Å^3 [37]. Similar values can be obtained for other instable valence elements like *5f*-Pu, for example.

The present study of $CeRh_{3-x}Pd_xB_{0.5}$ allows us to check these features directly because the Ce-V_{av} increases with Pd concentration whereas Z_{eff} deceases from 4+ to 3+, as indicated in figure 9. The figure summarizes the lattice parameters of the $AuCu_3$-unit cell as a function of the Pd-content for the alloys $ZrRh_{3-x}Pd_x$ [26], $CeRh_{3-x}Pd_x$ [2] and $CeAg_{3-z}Pd_z$ [2]. Notice that $CeRh_{3-x}Pd_xB_{0.5}$ refers to the upper *x*-axis, which is shifted by the equivalent of one Pd atom because, according to $Z_{eff} \times V_{av} =$ constant, the expansion produced by 0.5 B atoms is equivalent to such a variation in the electronic configuration of the conduction band. Three different regions are identified in the figure according to the Ce valence configurations: (i) a Ce^{4+} region on the left side, (ii) the Ce intermediate valence range around the middle of the phase diagram, and (iii) a Ce^{3+} one on the right side. A detailed analysis of each region follows.

(i) A linear increase of the unit cell dimensions throughout $ZrRh_{3-x}Pd_x$ essentially reflects the substitution of the smaller Rh atoms (metal radius $R_{Rh} = 0.1345$ nm [38]) by slightly larger Pd atoms ($R_{Pd} = 0.1376$ nm [38]) at a stable Zr^{4+} valency. Consistently, a similar slope ($\Delta'a'$ parameter/ΔPd-content) encountered on the Rh-rich side of $CeRh_{3-x}Pd_x$ up to

x_{Pd} <2.4 confirms a stable valency of the Ce^{4+} electronic configuration. The same applies to $CeRh_{3-x}Pd_xB_{0.5}$ after shifting the x_{Pd} concentration value to 1.5.

(ii) With higher Rh/Pd-substitution the intermediate valence region for Ce commences as documented by a series of physical properties. Interestingly, the isotypic Zr compound undergoes the mentioned structural modification at that Pd concentration. In the case of $CeRh_{3-x}Pd_x$, the Ce intermediate valence regime was explored beyond the $CePd_3$ limit [2, 12], revealing a further expansion of the unit cell when substituting Pd by Ag (R_{Ag} = 0.1445 nm [38]). This provides a further increase of carriers in the electronic band. Backed by measurements of specific heat, magnetic susceptibility and electrical resistivity [2], this further increase refers to the fact that in $CePd_3$, the Ce atom is still within its intermediate valence regime. For $CeRh_{3-x}Pd_xB_{0.5}$, the addition of band electrons allocated by Ag atoms is not required because of the 0.5 B content; the full range of Ce valence instability is developed within the Rh/Pd substitution range.

(iii) A plateau-like behavior is reached in $CeAg_{3-z}Pd_z$, indicating that at $z_{Pd} > 2.4$, Ce atoms have reached their Ce^{3+} regime. The same limit is reached for $CeRh_{3-x}Pd_xB_{0.5}$, but in this case at $x_{Pd} \approx 2.5$. Notably, no magnetic order is observed in this limit. For comparison, one can mention that $CePd_{2.58}Ag_{0.42}$ [2] also shows a divergent $C_m(T \to 0)/T$ dependence like the present Pd-rich samples, but does not reach such a high value.

5. Conclusions

The crystal structure and physical properties studied for the solid solution $CeRh_{3-x}Pd_xB_{0.5}$ have shown that the lattice expansion produced by B interstitial atoms increases the Ce valence to an extent that is nearly equivalent to the value obtained by increasing the concentration of one Pd atom in $Ce(Rh_{1-x}Pd_x)_3$. This indicates that both mechanisms generate a similar variation of the chemical potential of the system. Thus, the concentration dependence of Pd scales with the previously observed one for $Ce\{Rh,Pd,Ag\}_3$, as depicted in figure 9. As a consequence of the shift of the Pd content, produced by doping with 0.5 B atoms, the complete variation of the valence between Ce^{4+} and Ce^{3+} can be obtained solely by the Rh/Pd substitution, i.e., without any further increase of the number of electrons in the band, as created by a Pd/Ag substitution.

Having shifted the Ce^{3+} EC towards $CePd_3B_{0.5}$ facilitates access to the highest known density of low-energy excitations for a doublet ground-state system, with a value of $C_m/T \approx 4.4$ J mol^{-1} K^2 for $T \to 0$. The evolution from the Ce^{4+} to the Ce^{3+} configuration can be traced directly by the lattice parameter throughout three different regimes. For $0 \leqslant x \leqslant 1.5$ the volume increase corresponds merely to the substitution of Rh by Pd atoms, the sizes of which are rather close. In this regime, the tetravalent character of cerium is unaffected. This simple fact proves that each electronic configuration can be stable enough, requiring a significant modification of the electronic/volume environment in order to drive it into an intermediate valence regime.

For x >1.5, the lattice expansion is much steeper and is thus attributed to a gradual valence change of the cerium atoms, finally approaching a predominant trivalent state for $x > 2.4$. SAED patterns of the $CeRh_{3-x}Pd_xB_{0.5}$ compounds reveal the appearance of ½ ½ ½-type superstructures and satellite reflections with respect to the parent $AuCu_3$ structure. The former is

confined to the Rh-rich part of the solid solution, whereas the satellite reflections are observed throughout the solid solution and hint towards the existence of a domain structure enclosed by anti-phase boundaries.

This systematic investigation on the structural properties confirms that the extreme heavy fermion character of Pd-rich $CeRh_{3-x}Pd_xB_{0.5}$ alloys is an intrinsic property, rather than the consequence of atomic disorder. In fact, a slightly larger value of C_m/T ($T \to 0$) was obtained for $CePd_3B_{0.5}$ than figures reported in the literature for a similar B concentration [4, 5]. Also the description of the thermal dependence of C_m/T is improved using a simple modified power law function. The fact that a simple function describes C_m/T over a large temperature range indicates that only one dominant mechanism is involved. This excludes the presence of inhomogeneities in the sample which would contribute with different temperature dependences.

Acknowledgments

This work was supported by the Austrian Science Fund FWF under Grant P22295. I Z, J S and P R wish to thank the OEAD and the MINCyT for the research exchange through project AR22/2011. J S thanks the FOMCyT support through project PICT 1060-2010. All EPMA measurements were carried out in the Faculty Centre for Nanostructure Research at the University of Vienna.

References

[1] Harris I R, Norman M and Gardner W E 1972 *J. Less-Common Met.* **29** 299–309
[2] Mihalisin P, Scoboria P and Ward J A 1981 *Valence Fluctuations in Solids* eds L M Falicov, W Hanke and M B Maple (Amsterdam: North-Holand Pub. Co) p 61
[3] Perez I, Croft M, Liang G, Zhou J B, Shaheen S A and Jhans H 1987 *J. Appl. Phys.* **61** 3180
[4] Sereni J, Nieva G, Kappler J P, Besnus M J and Meyer A 1986 *J. Phys.* F*: Met. Phys.* **16** 435
[5] Sereni J G, Schmerber G and Kappler J P 2013 *IEEE Transaction on Magnetics* **49** 4647
[6] Dhar S K, Malik S K and Vijayaraghavan P R 1981 *Physical Review* B **10** 6182
[7] Malik S K, Dhar S K and Vijayaraghavan P R 1984 *Pramana* **22** 329
[8] Yubuta K, Nomura A, Nakaijma K and Shishido T 2006 *J. Alloys Compounds* **426** 308–11
[9] Holleck H 1971 *Conf. Digest - Institute of Physics* **3** London pp 109–12
[10] Joshi D A, Kumar N, Thamizhavel A and Dhar S K 2009 *Phys. Rev.* B*: Condens. Matter* **80** 224404–1
[11] Nieva G L 1988 *PhD Thesis* Instituto Balseiro, Universidad Nacional de Cuyo
[12] Gambke T, Elschner B, Schaafhausen J and Schaeffer H 1981 *Valence Fluctuations in Solids* eds L M Falicov, W Hanke and M B Maple (Amsterdam: North Holland) p 447
[13] Dhar S K, Gschneidner K A, Bredl C D and Steglich F 1989 *Phys. Rev.* B **39** 2439
[14] Kuentzler R, Dhar S K, Malik S K, Vijayaraghavan P R and Boqlin R 1984 *Solid State Commun.* **50** 145–50
[15] Wuilloudt E, Schneidert W D, Delley B, Baer Y and Hulliger F 1984 *J. Phys.* C*: Solid State Phys.* **17** 4799–806
[16] Sologub O, Rogl P, Salamakha L P, Bauer E, Hilscher G, Michor H and Giester G 2010 *J. Solid State Chem.* **183** 1013–37
[17] Lackner R, Bauer E and Rogl P 2006 *Physica* B **378–380** 835–6
[18] Jones C D W, Gordon R A, Cho B K, DiSalvo F J, Kim J S and Stewart G R 1999 *Phys.* B **262** 284–95
[19] Shishido T *et al* 2006 *J. Alloys Compd.* **426** 304–7
[20] Takei H and Shishido T 1984 *Less-Common Met.* **97** 223–9
[21] Yubuta K, Nomura A, Yamamura T and Shishido T 2008 *J. Alloys Compounds* **451** 301–4

[22] Hidenobu K, Ryoji S, Toestu S, Akiko N, Kunio K, Shigeru O, Vijay K, Kazuo N and Yoshiyuki K 2007 *Applied Phys. Lett.* **91** 081901
[23] Tay C Y and Harris I R 1977 *J. Less-Common Met.* **53** 177–92
[24] Beaurepaire E, Krill G, Kappler J P and Röhler J 1984 *Solid State Commun.* **49** 65
[25] Melnychenko-Koblyuk N *et al* 2007 *J. Phys. Condens. Matter* **19** 046203
[26] Pountney J M, Winterbottom J M and Harris I R 1978 *Inst. Phys. Conf. Ser.* **37** Chapter 385–91
[27] Massalski T B 1990 *Binary Alloy Phase Diagrams* 2nd edn (Materials Park, OH: ASM International) 1092–5
[28] Killer U, Scheidt E W, Scherer W, Michor H, Sereni J G, Pruschke T and Kehrien S 2004 *Phys. Rev. Lett.* **93** 216404
[29] Bock O and Müller U 2002 *Acta Cryst.* **B58** 594–606
[30] Hermus M and Fokwa B P T 2010 *J. Solid State Chem.* **183** 784–8
[31] Fokwa B P T, Eck B and Dronskowski R 2006 *Z. Kristallogr.* **221** 445–9
[32] Sereni J G 2007 *J. Low Temp. Phys.* **147** 179
[33] Sereni J G 1995 *Physica* B **215** 273
[34] Sereni J G 1991 *Handbook for the Physics and Chemistry of Rare Earths* vol 15, eds K A Gschneidner and L Eyring (Amsterdam: Elsevier) p 98
[35] Sereni J G, Geibel C, Berisso M G, Hellmann P, Trovarelli O and Steglich F 1997 *Physica* B **230** 580
[36] Löhneysen H V 1999 *J. Magn. Magn. Mat.* **200** 532–51
[37] Sereni J G 1982 *Proc. Valence Instabilities* eds E Wachter and T Boppart (Amsterdam: North Holland Pub. Co.) p 207
Sereni J G 1982 *J. Less Common Metals* **86** 287–98
[38] Taetum E, Gschneidner K and Waber J 1972 *The Crystal Chemistry and Physics of Metals and Alloys* ed W B Pearson (New York: Wiley Interscience)